Draft, Version 0.1
16th January 2019 4:45

Charm production in charged current deep inelastic scattering at HERA

ZEUS Collaboration

16th January 2019

Abstract

Charm production in charged current deep inelastic $e^{\pm}p$ scattering has been measured using data collected with the ZEUS detector at HERA representing an integrated luminosity of $358\,\mathrm{pb}^{-1}$. Results are presented separately for e^+p and e^-p scattering at a center-of-mass energy of $\sqrt{s} = 318\,\mathrm{GeV}$ within a kinematic phase space region of $200\,\mathrm{GeV}^2 < Q^2 < 60000\,\mathrm{GeV}^2$, $y < 0.9$, $E_T^{\mathrm{jet}} > 5\,\mathrm{GeV}$ and $-2.5 < \eta^{\mathrm{jet}} < 2.0$, where Q^2 is the squared four-momentum transfer, y is the inelasticity of the deep inelastic scattering, E_T^{jet} is the jet transverse energy and η^{jet} is the jet pseudorapidity. The visible charm jet cross sections were extrapolated from the visible to the full phase space region to determine the total charm cross sections. The electroweak part, $\sigma_{c^{EW}}$, of the charm cross sections were estimated with the help of MC calculations and found to be $\sigma^{+}_{c^{\mathrm{EW}}} = 11.8 \pm 7.7\,(\mathrm{stat.})\,^{+0.4}_{-2.0}\,(\mathrm{syst.})\,\mathrm{pb}$ in e^+p collisions and $\sigma^{-}_{c^{\mathrm{EW}}} = -8.0 \pm 10.0\,(\mathrm{stat.})\,^{+1.5}_{-1.7}\,(\mathrm{syst.})\,\mathrm{pb}$ in e^-p collisions.

1 Introduction

Measurements of heavy-flavour production serve as a good testing ground to investigate the predictive power of perturbative quantum chromodynamics (pQCD) as the large mass provides a natural hard scale for a wide range in phase space. While charm production in neutral current deep inelastic scattering (NC DIS) and in photoproduction have been extensively studied at HERA, this has not been done in charged current deep inelastic scattering (CC DIS) due to its small cross section.

In CC DIS, single charm quarks in the final state already occur at the level of the Quark Parton model (QPM) when either an incoming s or d quark is converted to a charm quark, or an incoming charm quark is converted to an s or d quark, as illustrated in Fig. 1 (a, b). In the latter case, the single charm in the event arises from the associated charm quark in the proton remnant. In addition, single charm can arise from a boson-gluon fusion (BGF) process producing a $c\bar{s}(c\bar{d})$ quark pair. In this case, the incoming virtual W boson "fuses" with a gluon from the proton which splits into a $s\bar{s}(d\bar{d})$ or $c\bar{c}$ pair in the initial state, as shown in Fig. 1 (c, d). All these processes lead to the same final state for either positrons or electrons:

$$e^+p \to \bar{\nu}_e c\bar{s}(\bar{d})X \qquad e^-p \to \nu_e \bar{c}s(d)X.$$

The characteristics of the events associated with the four subprocesses and their association to particular kinematic configurations in the final state depends on the QCD scheme chosen as detailed in the next section. The subreaction depicted in Fig. 1 (a) is directly sensitive to the strange quark content of the proton and can be used to constrain it. However, the extraction of the relevant part of the cross section is model dependent.

In the SU(3) flavour model, a perfect symmetry is assumed between the three light flavours, which results in equal quark densities for the sea quark components. This symmetry is broken if the strange quark density in the proton is suppressed by the mass of the strange quark, similar to the well-established strange quark suppression in fragmentation [1]. This mass-suppression, for larger values of Bjorken x, has been supported by experimental data such as the dimuon production in charged current by the CCFR [2] and NuTeV [3], as well as the NOMAD [4] and CHORUS [5] neutrino scattering experiments. However, the interpretation of these measurements depends on nuclear corrections and charm fragmentation and when these data are used by various parton distribution function (PDF) fitting groups no consensus has emerged on the exact level of suppression as a function of x. Additionally, the recent high-precision measurements of inclusive W and Z production by the ATLAS collaboration [6] report an unsuppressed strange sea in the low-x regime $x_{\mathrm{Bj}} < 0.05$. A similar result was obtained in a combined global QCD analysis of inclusive W and Z data from both the ATLAS and CMS experiments [7]. This observation was

also supported by the analysis of the ATLAS $W + c$ data [8]. However, the CMS $W + c$ data [9, 10] favour a somewhat smaller strangeness even at low-x values $x_{\mathrm{Bj}} \approx 0.02$.

A reevaluation of the LHC inclusive and $W + c$ measurements and the neutrino scattering measurements by NOMAD [4] and CHORUS [5] has been performed [11, 12], partly in an attempt to reconcile the factor-of-two discrepancy in the measured strange quark densities. The resulting strange-quark PDF was reported to be inconsistent with the ATLAS fit [6]. This is a compelling motivation to revisit this topic in order to improve the determination of the strange quark content in the proton. This paper presents measurements of charm production in CC DIS in $e^{\pm}p$ collisions using the data from the HERA II data-taking period exploiting the improved luminosity and particle identification capabilities from the HERA detector upgrade period [13, 14]. In order to contribute to the investigation, the electroweak contribution to charm production cross sections are compared with several QCD schemes which are detailed in the following section.

2 Charm production in CC DIS at HERA

The kinematics of lepton-proton scattering can be described in terms of the Lorentz-invariant variables x_{Bj}, y and Q^2. The variable Q^2 is the negative squared four-momentum of the exchange boson $-q^2 = -(k - k')^2$ where k and k' are the four-momenta of the incoming and outgoing lepton, respectively. The variable x_{Bj} is referred to as Bjorken x scaling variable and defined as $x_{\mathrm{Bj}} = \frac{Q^2}{2p \cdot q}$ where p is the four-momentum of the incoming proton. The variable y is the inelasticity of the DIS and defined as $y = \frac{p \cdot q}{p \cdot k}$.

The differential cross section at high Q^2 of charm production in CC DIS at HERA, mediated by a W boson, can be expressed in terms of the proton structure functions F_2, F_3 and F_L as follows [15]

$$\frac{d^2\sigma(e^{\pm}p \to \bar{\nu}_e(\nu_e)W^{\pm}X)}{dxdQ^2} = \frac{G_F^2}{4\pi x}\frac{M_W^4}{(Q^2 + M_W^2)^2}[Y_+F_2(x, Q^2) \mp Y_-xF_3(x, Q^2) - y^2F_L(x, Q^2)], \tag{1}$$

where G_F is the Fermi constant, M_W is the mass of the W boson and $Y_{\pm} = 1 \pm (1 - y)^2$. The longitudinal structure function F_L vanishes except at values of $y \approx 1$. The basic electroweak single charm production mechanisms were already described in the introduction. In the leading order plus parton shower Monte Carlo simulation (MC), the core electroweak matrix elements are based on the QPM graphs in Fig. 1 (a, b) and BGF-like configurations in Fig. 1 (c, d) through initial state parton showering. In addition, other tree-level higher order processes are also added through Leading Log (LL) parton showering. The electroweak matrix elements involving light quarks only are complemented by occasional final

state gluon splitting into $c\bar{c}$ pairs in the parton shower, with a semi-arbitrary cutoff mimicking charm mass effects. If only one of the two charm quarks (or its resulting hadron) is detected, and its charge is not measured (such as in the measurement technique used in this paper) then this "QCD" contribution is experimentally indistinguishable from electroweak production at the single event level. The experimental measurement thus refers to a sum of all these processes, which make differing contributions to different regions of phase space, but can not be disentangled with the presently available statistics.

In fixed order QCD calculations, the final state gluon splitting contribution in Fig. 2 is formally of next-to-next-to leading order (NNLO, $O(\alpha_s^2)$) and thus not included in the next-to-leading order (NLO, $O(\alpha_s)$) QCD predictions considered in this work, even though its contribution can be noticeable. QPM-like (Fig. 1 (a, b)) and BGF-like (Fig. 1 (c, d)) contributions are separated by the virtuality of the quark entering the electroweak process in relation to the chosen factorisation scale. NLO corrections to Fig. 1 (a, b) arise in the form of initial or final state gluon radiation, or a vertex correction.

In the zero-mass variable flavour number scheme (ZM-VFNS) [16, 17], the charm part of the structure functions F_2^c and xF_3^c can then be expressed in terms of different PDFs as follows

$$F_2^c = 2x\Big\{C_{2,q} \otimes \Big[|V_{cd}|^2\big(d+\bar{c}\big) + |V_{cs}|^2\big(s+\bar{c}\big)\Big] + 2\big(|V_{cd}|^2 + |V_{cs}|^2\big)C_{2,g} \otimes g\Big\}, \quad (2)$$

$$xF_3^c = 2x\Big\{C_{3,q} \otimes \Big[|V_{cd}|^2\big(d-\bar{c}\big) + |V_{cs}|^2\big(s-\bar{c}\big)\Big] + \big(|V_{cd}|^2 + |V_{cs}|^2\big)C_{3,g} \otimes g\Big\}, \quad (3)$$

in e^+p collisions, and

$$F_2^c = 2x\Big\{C_{2,q} \otimes \Big[|V_{cd}|^2\big(\bar{d}+c\big) + |V_{cs}|^2\big(\bar{s}+c\big)\Big] + 2\big(|V_{cd}|^2 + |V_{cs}|^2\big)C_{2,g} \otimes g\Big\}, \quad (4)$$

$$xF_3^c = 2x\Big\{C_{3,q} \otimes \Big[|V_{cd}|^2\big(-\bar{d}+c\big) + |V_{cs}|^2\big(-\bar{s}+c\big)\Big] + \big(|V_{cd}|^2 + |V_{cs}|^2\big)C_{3,g} \otimes g\Big\}, \quad (5)$$

in e^-p collisions, where $C_{i,j}$ is the coefficient function for parton j in structure function F_i and d, s, c and g are respectively the down, strange, charm and gluon PDFs with the argument (x, Q^2) omitted. $|V_{ij}|$ are the Cabbibo matrix elements, given by PDG [1] as

$$V = \begin{bmatrix} |V_{ud}| & |V_{us}| & |V_{ub}| \\ |V_{cd}| & |V_{cs}| & |V_{cb}| \\ |V_{td}| & |V_{ts}| & |V_{tb}| \end{bmatrix} \approx \begin{bmatrix} 0.97 & 0.22 & 0.0039 \\ 0.22 & 1.0 & 0.042 \\ 0.0081 & 0.039 & 1.0 \end{bmatrix}. \quad (6)$$

Furthermore, part of the effects beyond NLO are resummed at next-to-leading log in the zero-mass approximation.

In the NLO Fixed Flavour Number (FFN) scheme [18, 19], charm mass effects are treated explicitly up to $O(\alpha_s)$ in the matrix elements. In this scheme, there is no charm quark content in the proton, thus the charm QPM graph in Fig. 1 (b) and its associated higher order corrections do not occur. This is compensated by a correspondingly larger gluon content in the proton, such that all initial state charm contributions irrespective of scale are treated explicitly in the BGF matrix element (Fig. 1 (d)). No resummation is performed.

In the FONLL-B scheme [20, 21], a general mass heavy flavour number scheme (GM-VFNS), charm mass effects are accounted for by interpolating between the ZM-VFNS and FFN predictions, such that all mass effects are correctly included up to $O(\alpha_s)$, while NLL resummation of higher orders remains in the massless approximation.

3 Experimental set-up

This analysis was performed with data taken during the HERA II data-taking period in the years 2003-2007. During this period, electrons and positrons with an energy of 27.5 GeV collided with protons with an energy of 920 GeV at a centre-of-mass energy of $\sqrt{s} = 318\,\text{GeV}$. The corresponding integrated luminosities are $173\,\text{pb}^{-1}$ and $185\,\text{pb}^{-1}$ for e^+p and e^-p collisions, respectively.

A detailed description of the ZEUS detector can be found elsewhere [22]. A brief outline of the components that are most relevant for this analysis is given below.

In the kinematic range of the analysis, charged particles were tracked in the central tracking detector (CTD) [23], the microvertex detector (MVD) [13] and the STT [24]. The CTD and the MVD operated in a magnetic field of 1.43 T provided by a thin superconducting solenoid. The CTD drift chamber covered the polar-angle[1] region $15^\circ < \theta < 164^\circ$. The MVD silicon tracker consisted of a barrel (BMVD) and a forward (FMVD) section. The BMVD provided polar angle coverage for tracks with three measurements from 30° to 150°. The FMVD extended the polar-angle coverage in the forward region to 7°. The STT covered the polar-angle region $5^\circ < \theta < 25^\circ$.

The high-resolution uranium–scintillator calorimeter (CAL) [25] consisted of three parts: the forward (FCAL), the barrel (BCAL) and the rear (RCAL) calorimeters. Each part was subdivided transversely into towers and longitudinally into one electromagnetic section (EMC) and either one (in RCAL) or two (in BCAL and FCAL) hadronic sections (HAC). The smallest subdivision of the calorimeter was called a cell. The CAL energy resolutions,

[1] The ZEUS coordinate system is a right-handed Cartesian system, with the Z axis pointing in the nominal proton beam direction, referred to as the "forward direction", and the X axis pointing towards the centre of HERA. The coordinate origin is at the centre of the CTD. The pseudorapidity is defined as $\eta = -\ln\left(\tan\frac{\theta}{2}\right)$, where the polar angle, θ, is measured with respect to the Z axis.

as measured under test-beam conditions, were $\sigma(E)/E = 0.18/\sqrt{E}$ for electrons and $\sigma(E)/E = 0.35/\sqrt{E}$ for hadrons, with E in GeV.

The iron yoke surrounding the CAL was instrumented with proportional drift chambers to form the Backing Calorimeter (BAC) [26]. The BAC consisted of 5142 aluminium chambers inserted into the gaps between 7.3 cm thick iron plates (10, 9 and 7 layers in forecap, barrel and rearcap, respectively) serving as calorimeter absorber. The chambers were typically 5 m long and had a wire spacing of 1.5 cm. The anode wires were covered by 50 cm long cathode pads. The BAC was equipped with energy readout and position sensitive readout for muon tracking. The former was based on 1692 pad towers (50×50 cm^2), providing an energy resolution of $\sim 100\,\%/\sqrt{E}$, with E in GeV. The position information from the wires allowed the reconstruction of muon trajectories in two dimensions (XY in barrel and YZ in endcaps) with spatial accuracy of a few mm.

The luminosity was measured using the Bethe-Heitler reaction $ep \to e\gamma p$ by a luminosity detector which consisted of independent lead-scintillator calorimeter [27] and magnetic spectrometer [28] systems. The fractional systematic uncertainty on the measured luminosity was 2.6 %.

4 Monte Carlo simulation

Inclusive CC DIS samples were used to simulate charm signal and light-flavour (LF) background events. Neutral current DIS and photoproduction samples were used to simulate non-CC DIS backgrounds, which were found to be negligible after the CC selection defined below. The charged current events were generated with DJANGOH 1.6 [29], using CTEQ5D PDF sets [30] including QED and QCD radiative effects at the parton level. The ARIADNE 4.12 color-dipole model [31] was used for the fragmentation simulation. The Lund string model was used for hadronization, as implemented in JETSET 7.4.1 [32]. The NC DIS events and photoproduction events were simulated by using DJANGOH and HERWIG 5.9 [33], respectively.

5 Event selection and reconstruction

5.1 Reconstruction of kinematic variables

CC DIS at HERA produces a neutrino in the final state. The neutrino then escapes the ZEUS detector, resulting in a loss of information on the leptonic final state. Thus, the Lorentz-invariant kinematic variables must be defined with the hadronic final state. In the present analysis, this is done via the Jacquet–Blondel method, which requires the four-momentum of the exchange boson q to be equal not only to the variation in leptonic

four-momentum $k - k'$ but also to the variation in hadronic four-momentum $p - p'$. Then, the invariant variables described in Section 1 can be defined as follows

$$y_{\rm JB} = \frac{\sum_h (E - p_z)_h}{2E_{e,\rm beam}}, \tag{7}$$

$$Q^2_{\rm JB} = \frac{p^2_{T,h}}{1 - y_{\rm JB}}, \tag{8}$$

$$x_{\rm JB} = \frac{Q^2_{\rm JB}}{2s y_{\rm JB}}, \tag{9}$$

where s is the center-of-mass energy of the collision. The difference between the true and reconstructed kinematic variables was found to be within $\sim 1\%$ in the MC simulation study.

5.2 DIS selection

The ZEUS online three-level trigger system loosely selected CC DIS candidates based on calorimeter and tracking information [34, 35]. The surviving events were then required to pass the following offline selection criteria to reject non-CC DIS events:

- a kinematic selection cut was implemented at $200\,\text{GeV}^2 < Q^2_{\rm JB} < 60000\,\text{GeV}^2$ and $y_{\rm JB} < 0.9$ to confine the sample into a region with the optimal resolution of the kinematic quantities and small background;
- a characteristic of CC DIS events is the large missing transverse momentum $p_{T,\rm miss}$ in the calorimeter due to the final state neutrino. Events were required to have $p_{T,\rm miss} > 12\,\text{GeV}$ and $p'_{T,\rm miss} > 10\,\text{GeV}$ where $p'_{T,\rm miss}$ is the missing transverse momentum, excluding measurements taken from the CAL cells adjacent to the forward beam hole;
- further background rejection is discussed in detail in a dedicated study of CC DIS at ZEUS in the e^+p scattering periods [36]. In addition, the remaining cosmic muons are removed by requiring the number of hits in the calorimeter cells $N_{\rm cell} > 40$ and comparing the fraction of energy deposited in the EMC and HAC. The rear-hitting events with the energy deposited in the RCAL $E_{\rm RCAL} > 2\,\text{GeV}$ were rejected if $E_{\rm RHAC}/E_{\rm RCAL} > 0.5$. The barrel-hitting events with the energy in the BCAL, $E_{\rm BCAL} > 2\,\text{GeV}$, were rejected if $E_{\rm BHAC}/E_{\rm RCAL} > 0.85$, $E_{\rm BHAC1}/E_{\rm RCAL} > 0.7$ or $E_{\rm BHAC2}/E_{\rm RCAL} > 0.4$. The forward-hitting events with the energy in the FCAL, $E_{\rm FCAL} > 2\,\text{GeV}$, were rejected if $E_{\rm FHAC}/E_{\rm FCAL} < 0.1$, $E_{\rm FHAC}/E_{\rm FCAL} > 0.85$, $E_{\rm FHAC1}/E_{\rm FCAL} > 0.7$ or $E_{\rm FHAC2}/E_{\rm FCAL} > 0.6$.

A total of 4093 events in e^+p data and 8895 in e^-p data passed these selection criteria. Comparisons of data and MC at the event level selection stage are shown in Fig. 3 and 4 for e^+p and e^-p, respectively. The MC distribution is consistent with data in both the e^+p and e^-p periods. From MC studies, the charm contribution to the CC events is about 25% in the e^+p periods and 12% in the e^-p periods in relative terms, and similar for both periods in absolute terms.

5.3 Charm selection and signal extraction

Charm quarks in CC DIS events were tagged by using an inclusive lifetime method [37, 38]. In CC DIS at HERA, LF production has the highest production rate and thus contributes as the major source of background. The lifetime method uses the decay length of the secondary interaction vertex as a distinguishing variable to suppress this background contribution. The underlying principle of this method is that ground state heavy-flavoured (HF) particles typically have a longer lifetime than LF particles and travel a longer distance before they decay at a secondary interaction vertex.

Jets were reconstructed with the k_T clustering algorithm in the massive mode [39–41] and were required to satisfy the following criteria:

- $E_T^{\rm jet} > 5\,{\rm GeV}$,
- $-2.5 < \eta^{\rm jet} < 2.0$ (1.5),

where $E_T^{\rm jet}$ is the jet transverse energy and $\eta^{\rm jet}$ is the pseudorapidity. The tracking efficiency and resolution in the forward region $\eta^{\rm jet} > 1.5$ suffered in the 2005 data-taking period as the STT was turned off during this time (e^-p). Thus, the jets from this period were required to satisfy a tighter $\eta^{\rm jet}$ upper limit $\eta^{\rm jet} < 1.5$. These selection criteria constrain the kinematic phase space region of this analysis, along with the kinematic selection criteria at the event level selection stage. Secondary interaction vertices were reconstructed when there were more than two tracks associated with the chosen jet. They were required to satisfy the following criteria.

- $N_{\rm secvtx}^{\rm trk} \geq 3$,
- $\chi^2/N_{dof} < 6$,
- $|z_{\rm secvtx}| < 30$ cm,
- $M_{\rm secvtx} < 6\,{\rm GeV}$,
- $\sqrt{\Delta x^2 + \Delta y^2} < 1$ cm,

where $N^{\mathrm{trk}}_{\mathrm{secvtx}}$ is the number of tracks used to reconstruct the vertex, χ^2/N_{dof} is the goodness of the vertex fitting, z_{secvtx} is the Z-coordinate of the secondary vertex, M_{secvtx} is the hadronic mass of the secondary vertex and Δx and Δy are the X- and Y-displacement of the secondary vertex from the primary interaction vertex. These selection criteria ensure a good fit quality and high acceptance of the CTD and MVD for tracks used to reconstruct the vertices. The requirement on the track multiplicity was implemented in order to minimize the number of "fake" vertices reconstructed in the vertex detector which has the highest rate when reconstructed with two tracks. Figure 5 and 6 show the distributions of the chosen jets and secondary vertices in the e^+p and e^-p periods, respectively.

The transverse decay length of the selected secondary interaction vertices was projected onto its corresponding jet axis. Due to the finite resolution of the MVD and the short decay length of LF particles, the 2D decay length (L_{xy}) and the significance of the decay length ($S = L_{xy}/\delta_{L_{xy}}$) distributions of LF particles were symmetric, whereas the distributions of HF particles, in this case charmed particles, were asymmetric, as illustrated in Figures 7 and 8 (a, b). Consequently, the LF background was suppressed by subtracting the negative decay length distribution from the positive decay length distribution. The region around $|L_{xy}| = 0$ or $|S| = 0$ was dominated by the statistical uncertainty from the high symmetry of light-flavoured distribution after the subtraction. To ensure low statistical uncertainty in the extracted signal, vertices were required to satisfy an absolute significance threshold. The exact value of the threshold was determined so that the signal significance is expected to be the highest and found to be at $|S| = 2$. Figures 7 and 8 (c, d) illustrate the shape of the variables after the background subtraction. The surviving events after the decay length subtraction were used to extract charm cross section in two bins in Q^2.

6 Charm cross section

The lifetime method used in this analysis tags charm quarks regardless of their origin. Thus, the selected reactions include charm production from the final state gluon splitting, such as the one in Fig. 2, which is here denoted by QCD charm, in addition to the electroweak charm (EW charm) production discussed in Section 2. In the present analysis, charm production was measured inclusively within the visible phase space region of $200\,\mathrm{GeV}^2 < Q^2 < 60000\,\mathrm{GeV}^2$, $y < 0.9$, $E_T^{\mathrm{jet}} > 5\,\mathrm{GeV}$ and $-2.5 < \eta^{\mathrm{jet}} < 2.0$. No attempt was made to experimentally disentangle the different theoretical contributions as the limited statistics and non-measurement of the charm quark charge did not allow doing so. The visible charm jet cross sections $\sigma_{c,\mathrm{vis}}$ were initially measured as follows

$$\sigma_{c,\mathrm{vis}} = \frac{M^{\mathrm{data}} - M^{\mathrm{MC}}_{\mathrm{bg}}}{M^{\mathrm{MC}}_{c}} \cdot \sigma^{\mathrm{MC}}_{c,\mathrm{vis}}, \tag{10}$$

where M^{data} is the reconstructed number of charm jet candidates in the data after the decay length subtraction, $M_{\text{bg}}^{\text{MC}}$ is the background contribution estimated from the MC and M_c^{MC} is the estimatated charm/anti-charm contribution expected from the MC. $\sigma_{c,\text{vis}}^{\text{MC}}$ is the cross section of jets that are generated in the MC within the kinematic region and associated to a generated charm or anti-charm quark when $\sqrt{\Delta\phi^2 + \Delta\eta^2} < 1$ where $\Delta\phi$ and $\Delta\eta$ are respectively the azimuthal-angle and pseudorapidity difference between the jet and charm quark. Each charm quark was evaluated individually against each jet when more than one charm quark and jet were generated. In this case, all jets within the visible phase space region and associated with a charm quark were measured.

The EW contribution in the charm quark signal $\sigma_{c^{\text{EW}},\text{vis}}$ could be isolated by subtracting the QCD contribution from gluon splitting shown in Fig. 2. However, the available prediction from ARIADNE 4.12, like any prediction from gluon splitting in the massless mode with arbitrary cutoff, cannot be considered to be reliable, and might be overestimated. As it is expected to be small (Table 3) it is assumed to vanish for the central result but considered as a systematic uncertainty. The visible jet cross section was extrapolated to the full kinematic phase space region via an extrapolation factor C_{ext} which was estimated from the ratio between the number of charm events generated in the MC, $N_{\text{gen}}^{\text{EW}}$, and the charm jet within the kinematic region, $N_{\text{kin}}^{\text{EW}}$:

$$C_{\text{ext}} = \frac{N_{\text{gen}}^{\text{EW}}}{N_{\text{kin}}^{\text{EW}}}. \tag{11}$$

The resulting total EW charm cross section $\sigma_{c^{\text{EW}}}$ is then given by

$$\begin{aligned} \sigma_{c^{\text{EW}}} &= C_{\text{ext}}\ \sigma_{c,\text{vis}} \\ &= \frac{N_{\text{gen}}^{\text{EW}}}{N_{\text{kin}}^{\text{EW}}}\ \frac{M^{\text{data}} - M_{\text{bg}}^{\text{MC}}}{M_c^{\text{MC}}}\ \sigma_{c,\text{vis}}^{\text{MC}}. \end{aligned} \tag{12}$$

7 Systematic Uncertainties

Systematic uncertainties from the following sources have been estimated in this analysis. Below is the list of the sources of uncertainty and their estimated effects to the total EW charm cross sections provided in parentheses ($\delta\sigma^{e^+p}$, $\delta\sigma^{e^-p}$):

- δ_{1a} CC DIS (negligible) and δ_{1b} secondary vertex (+2.0 pb, +4.0 pb) selection
  The uncertainty associated with the exact values of the selection criteria were evaluated in a previous analysis of CC DIS at HERA using the ZEUS detector [42]. This was done by varying the selection criteria thresholds by a fraction and repeating

the charged current cross section measurement. The uncertainty in the secondary interaction vertex selection method was estimated by lifting the restriction on the secondary vertex track multiplicity $N^{\mathrm{trk}}_{\mathrm{secvtx}}$.

- δ_2 Calorimeter (negligible)
  The uncertainty in E_T^{jet} measurement due to imperfect calibration of hadronic calorimeter at ZEUS is known to be $\pm 3\%$. The uncertainty associated with this effect was estimated by varying the E_T^{jet} cut by $\pm 3\%$ in the MC and repeating the measurement.

- δ_3 LF background (negligible)
  Some LF particles such as K meson and Λ baryon typically have a lifetime comparable to HF particles. Some of these longer-lived LF particles might survive the decay length subtraction. The uncertainty in the remaining LF background was estimated by varying the LF background by $\pm 30\%$.

- δ_4 EW charm fraction ($-0.8\,\mathrm{pb},\ -1.6\,\mathrm{pb}$)
  The MC predictions of the QCD contribution (Fig. 2) shown in Table 3 of $+6\%$ for e^+p collisions and $+12\%$ for e^-p collisions were taken as systematic uncertainty.

- δ_5 Secondary vertex rescaling ($-1.8\,\mathrm{pb},\ +1.4\,\mathrm{pb}$)
  The MC samples used in this analysis appear to have a better efficiency in detecting secondary vertices than data. A secondary normalization factor was applied to the MC vertex distributions. This normalization was performed only to the LF background distribution to test different hypothesis for its origin.

- δ_6 Signal extraction ($\pm 6.2\,\mathrm{pb},\ \pm 3.8\,\mathrm{pb}$)
  A high fluctuation in the signal is observed around the significance threshold. In order to decouple the systematic uncertainty from the statistical effect, the cross-section measurement was repeated multiple times with varying significance threshold values and evaluated against a linear fit. The systematic uncertainty was estimated as the value of the fit at $S_{\mathrm{thresh}} = S_{\mathrm{nominal}} \pm 1$.

- Luminosity
  Uncertainty in ZEUS luminosity measurement is $\pm 2\%$. It was neglected in the final plots.

Attempts were made to separate the systematic uncertainties evaluated at the cross section calculation stage of the measurement, δ_6 in particular, from the statistical effect. However, this has proven to be ineffective as the uncertainty of the linear fit was comparable to the listed systematic uncertainty. Thus, the δ_6 and δ_{1b}, also found to be difficult to correctly estimate, were not included in the total systematic uncertainty in the following section.

8 Results

The charm jet cross sections in CC DIS in $e^{\pm}p$ collisions were measured in the visible kinematic phase space of $200\,\text{GeV}^2 < Q^2 < 60000\,\text{GeV}^2$, $y < 0.9$, $E_T^{\text{jet}} > 5\,\text{GeV}$ and $-2.5 < \eta^{\text{jet}} < 2.0$ to be

$$\begin{aligned}\sigma^{+}_{c,\text{vis}} &= 4.0 \pm 2.8\ (\text{stat.})\ ^{+0.1}_{-0.6}\ (\text{syst.})\ \text{pb},\\ \sigma^{-}_{c,\text{vis}} &= -3.0 \pm 3.8\ (\text{stat.})\ ^{+0.5}_{-0.1}\ (\text{syst.})\ \text{pb},\end{aligned}$$

where the superscript $\pm$ denotes the charge of the incoming lepton. A comparison of the data and MC in bins of Q^2 is shown in Fig. 9. The QCD contribution to charm production was introduced as systematic uncertainty in the electroweak part of the charm cross sections. The EW charm jet cross sections in consideration of this uncertainty are given by

$$\begin{aligned}\sigma^{+}_{c^{\text{EW}},\text{vis}} &= 4.0 \pm 2.8\ (\text{stat.})\ ^{+0.1}_{-0.6}\ (\text{syst.})\ \text{pb},\\ \sigma^{-}_{c^{\text{EW}},\text{vis}} &= -3.0 \pm 3.8\ (\text{stat.})\ ^{+0.5}_{-0.6}\ (\text{syst.})\ \text{pb}.\end{aligned}$$

The total electroweak charm cross sections were found by extrapolating the visible EW charm jet cross sections to the full kinematic phase space to be

$$\begin{aligned}\sigma^{+}_{c^{\text{EW}}} &= 11.8 \pm 7.7\ \ (\text{stat.})\ ^{+0.4}_{-2.0}\ (\text{syst.})\ \text{pb},\\ \sigma^{-}_{c^{\text{EW}}} &= -8.0 \pm 10.0\ (\text{stat.})\ ^{+1.5}_{-1.7}\ (\text{syst.})\ \text{pb}.\end{aligned}$$

The corresponding extrapolation factors $C^{\pm}_{\text{ext}}$ were found in the MC to be

$$\begin{aligned}C^{+}_{\text{ext}} &= 2.78,\\ C^{-}_{\text{ext}} &= 2.67.\end{aligned}$$

A comparison of the theory predictions in the FFN and FONLL-B schemes, MC and data in bins of Q^2 is shown in Fig. 10. The total uncertainty of the FONLL-B scheme is obtained by adding in quadrature the PDF, scale and charm mass uncertainties and represented in the plot as a band around the central value. Table 1 provides the experimental values of the cross sections $\sigma_{c,\text{vis}}$, $\sigma_{c^{\text{EW}},\text{vis}}$ and $\sigma_{c^{\text{EW}}}$ for each bin in Q^2. The contributions of the charm production subprocesses to the final EW cross section in each bin were estimated in the MC, FFN and FONLL-B predictions and listed in Table 2. The contributions of the

subprocesses including the final gluon splitting described in Fig. 2 to the MC-generated charm signal in the visible and full kinematic range were provided in Table 3. In Table 4 are shown the theory predictions from FFN and FONLL schemes with the total uncertainties and ZM-VFNS scheme with varied strange quark fraction $f_s = \frac{\bar{s}}{\bar{d}+\bar{s}}$.

The FFN scheme predictions were generated with OPENQCDRAD [43] using the ABMP 16.3 NLO PDF sets [44, 45]. The FONLL-B predictions were generated by using the APFEL [46] with NNPDF3.1 [47]. The ZM-VFNS predictions were generated with HERAPDF2.0 [48]. The variation of f_s was chosen to span the ranges between a suppressed strange sea [49,50] and an unsuppressed strange sea [6, 51]. In addition to this, two more variations of the assumptions about the strange sea were made. Instead of assuming that the strange contribution is a fixed fraction of the d-type sea, an x-dependent shape, $x\bar{s} = f'_s\, 0.5 \tanh(-20(x - 0.07))\, x\bar{D}$ where $x\bar{D} = x\bar{d} + x\bar{s}$, was used in which high-x strangeness is highly suppressed. This was suggested by measurements published by the HERMES collaboration [52, 53]. The normalisation of f'_s was also varied between $f'_s = 0.3$ and $f'_s = 0.5$. The ZM-VFNS prediction was also evaluated with the ATLAS-$epWZ16$ PDF sets [6], a new PDF sets that supersedes ATLAS-$epWZ12$ sets. The xFitter framework was used to interface the theoretical predictions [54].

The theory predictions in Table 2 suggest that the QPM process described in Fig. 1 (a) contributes to the final EW cross section about 30 $\sim$ 50% depending on the kinematic range and QCD scheme used. The increase in the QPM contribution and the decrease in the BGF contribution from the visible to the full kinematic range shown in Table 3 hint that a portion of charm quarks originated from the BGF processes escaped through the beam pipe. In general, the data are well described by the theory predictions within the experimental uncertainty. The result from e^-p collisions, in particular, leaned toward a somewhat low EW charm cross section which favours a smaller strange quark content. The large statistical uncertainty, however, rendered the measurement insensitive to the quantitative evaluation of the choice of different QCD schemes or the variation in the assumptions about the strange quark content.

9 Summary and conclusions

Measurements of charm production in charged current deep inelastic scattering in $e^{\pm}p$ collisions have been performed based on HERA II data with an integrated luminosity of $358\,\mathrm{pb}^{-1}$, which corresponds to e^+p collisions of an integrated luminosity of $173\,\mathrm{pb}^{-1}$ and e^-p collisions of an integrated luminosity of $185\,\mathrm{pb}^{-1}$. Visible EW charm jet cross sections for each lepton beam type were measured within a kinematic region, $200\,\mathrm{GeV}^2 < Q^2 < 60000\,\mathrm{GeV}^2$, $y < 0.9$, $E_T^{\mathrm{jet}} > 5\,\mathrm{GeV}$ and $-2.5 < \eta^{\mathrm{jet}} < 2.0$, and extrapolated to the full kinematic range. Theoretical predictions with several assumptions about the strange quark content and using different heavy flavour schemes were found to be consistent with

the data within the large experimental uncertainties. The analysis presented here shows the potential of DIS measurements to increase the knowledge about the strange quark content of the proton. However, the HERA data lack statistics by about two orders of magnitude to be decisive on the subject. In future lepton-ion collider projects, such as the US-based electron-ion collider [55], this can be overcome by higher luminosity and detectors equipped with better vertex detection resolution.

Acknowledgements

We appreciate the contributions to the construction, maintenance and operation of the ZEUS detector of many people who are not listed as authors. The HERA machine group and the DESY computing staff are especially acknowledged for their success in providing excellent operation of the collider and the data-analysis environment. We thank the DESY directorate for their strong support and encouragement.

References

[1] M. Tanabashi et al., Phys. Rev. **D98**, 030001 (2018).

[2] M. Goncharov et al., Phys. Rev. **D64**, 112006 (2001).

[3] CCFR Collab., A. O. Bazarko et al., Z. Phys. **C65**, 189 (1995).

[4] O. Samoylov et al., Nucl. Phys. **B876**, 339 (2013).

[5] A. Kayis-Topaksu et al., New J. Phys. **13**, 093002 (2011).

[6] ATLAS Collab., M. Aaboud et al., Eur. Phys. J. **C77**, 367 (2017).

[7] A. Cooper-Sarkar and K. Wichmann, Phys. Rev. **D98**, 014027 (2018).

[8] ATLAS Collab., G. Aad et al., JHEP **05**, 068 (2014).

[9] CMS Collab., S. Chatrchyan et al., JHEP **02**, 013 (2014).

[10] CMS Collab., S. Chatrchyan et al., submitted EPJC.

[11] S. Alekhin et al., Phys. Rev. **D91**, 094002 (2015).

[12] S. Alekhin et al., Phys. Lett. **B777**, 134 (2018).

[13] A. Polini et al., Nucl. Instr. and Meth. **A 581**, 656 (2007).

[14] U. Schneekloth, DESY-HERA-98-05 (1998).

[15] R. Devenish and A. Cooper-Sarkar, *Deep Inelastic Scattering*. Oxford University Press, 2003.

[16] R. S. Thorne and R. G. Roberts, Eur. Phys. J. **C19**, 339 (2001).

[17] Cooper-Sarkar, Amanda M. and Devenish, R. C. E. and De Roeck, A., Int. J. Mod. Phys. **A13**, 3385 (1998).

[18] E. Laenen et al., Nucl. Phys. **B392**, 162 (1993).

[19] S. Alekhin et al., Phys. Rev. **D81**, 014032 (2010).

[20] M. Cacciari, M. Greco and P. Nason, JHEP **05**, 007 (1998).

[21] S. Forte et al., Nucl. Phys. **B834**, 116 (2010).

[22] ZEUS Collab., U. Holm (ed.), *The ZEUS Detector*. Status Report (unpublished), DESY (1993). `http://www-zeus.desy.de/bluebook/bluebook.html`.

[23] N. Harnew et al., Nucl. Instr. and Meth. **A 279**, 290 (1989);
B. Foster et al., Nucl. Phys. Proc. Suppl. **B 32**, 181 (1993);
B. Foster et al., Nucl. Instr. and Meth. **A 338**, 254 (1994).

[24] S. Fourletov, Nucl. Instr. and Meth. **A 535**, 191 (2004).

[25] M. Derrick et al., Nucl. Instr. and Meth. **A 309**, 77 (1991);
A. Andresen et al., Nucl. Instr. and Meth. **A 309**, 101 (1991);
A. Caldwell et al., Nucl. Instr. and Meth. **A 321**, 356 (1992);
A. Bernstein et al., Nucl. Instr. and Meth. **A 336**, 23 (1993).

[26] I. Kudla et al., Nucl. Instr. and Meth. **A 300**, 480 (1991).

[27] J. Andruszków et al., Preprint DESY-92-066, DESY, 1992;
ZEUS Collab., M. Derrick et al., Z. Phys. **C 63**, 391 (1994);
J. Andruszków et al., Acta Phys. Pol. **B 32**, 2025 (2001).

[28] M. Helbich et al., Nucl. Instr. and Meth. **A 565**, 572 (2006).

[29] H. Spiesberger, DJANGO1.6 *Version 4.6.6 – A Monte Carlo Generator for Deep Inelastic Lepton Proton Scattering Including QED and QCD Radiative Effects*, 2005. `http://wwwthep.physik.uni-mainz.de/~hspiesb/djangoh/djangoh.html`.

[30] H. L. Lai et al., Eur. Phys. J. **C12**, 375 (2000).

[31] L. Lonnblad, Comput. Phys. Commun. **71**, 15 (1992).

[32] T. Sjostrand, Comput. Phys. Commun. **82**, 74 (1994).

[33] G. Marchesini et al., Comput. Phys. Commun. **67**, 465 (1992).

[34] W. H. Smith, K. Tokushuku and L. W. Wiggers, *Proc. Computing in High-Energy Physics (CHEP), Annecy, France, Sept 21-25, 1992*, pp. 222–225. (1992).

[35] P. D. Allfrey et al., Nucl. Instrum. Meth. **A580**, 1257 (2007).

[36] ZEUS Collab., H. Abramowicz et al., Eur. Phys. J. **C70**, 945 (2010).

[37] ZEUS Collab., S. Chekanov et al., Eur. Phys. J. **C63**, 171 (2009).

[38] H1 Collab., F. D. Aaron et al., Eur. Phys. J. **C65**, 89 (2010).

[39] S. Catani, Y. L. Dokshitzer and B. R. Webber, Phys. Lett. **B285**, 291 (1992).

[40] S. Catani et al., Nucl. Phys. **B406**, 187 (1993).

[41] S. D. Ellis and D. E. Soper, Phys. Rev. **D48**, 3160 (1993).

[42] ZEUS Collab., S. Chekanov et al., Eur. Phys. J. **C32**, 1 (2003).

[43] *OPENQCDRAD*, `http://www-zeuthen.desy.de/~alekhin/OPENQCDRAD`.

[44] S. Alekhin, J. Blumlein and S. Moch, Phys. Rev. **D86**, 054009 (2012).

[45] I. Bierenbaum, J. Blumlein and Klein, Phys. Lett. **B672**, 401 (2009).

[46] V. Bertone, S. Carrazza and J. Rojo, Comput. Phys. Commun. **185**, 1647 (2014).

[47] R. D. Ball et al., Eur. Phys. J. **C77**, 663 (2017).

[48] H1 and ZEUS Collabs., H. Abramowicz et al., Eur. Phys. J. **C75**, 580 (2015).

[49] A. D. Martin et al., Eur. Phys. J. **C63**, 189 (2009).

[50] P. M. Nadolsky et al., Phys. Rev. **D78**, 013004 (2008).

[51] ATLAS Collab., G. Aad, et al., Phys. Rev. Lett. **109**, 012001 (2012).

[52] HERMES Collab. A. Airapetian et al., Phys. Lett. **B666**, 446 (2008).

[53] HERMES Collab. A. Airapetian et al., Phys. Rev. **D89**, 097101 (2014).

[54] S. Alekhin et al., Eur. Phys. J. **C75**, 304 (2015).

[55] A. Accardi et al., Eur. Phys. J. **A52**, 268 (2016).

Q^2 range (GeV^2)	$\sigma_{c,\mathrm{vis}}$(pb)				
e^+p					
200–1500	4.1	± 2.0	(stat.)	$^{+0.1}_{-0.6}$	(syst.)
1500–60000	-0.7	± 2.0	(stat.)	$^{+0.2}_{-0.0}$	(syst.)
e^-p					
200–1500	-0.9	± 2.1	(stat.)	$^{+0.2}_{-0.0}$	(syst.)
1500–60000	-2.6	± 3.5	(stat.)	$^{+0.5}_{-0.1}$	(syst.)
Q^2 range (GeV^2)	$\sigma_{c^{\mathrm{EW}},\mathrm{vis}}$(pb)				
e^+p					
200–1500	4.1	± 2.0	(stat.)	$^{+0.1}_{-0.6}$	(syst.)
1500–60000	-0.7	± 2.0	(stat.)	$^{+0.2}_{-0.1}$	(syst.)
e^-p					
200–1500	-0.9	± 2.1	(stat.)	$^{+0.2}_{-0.2}$	(syst.)
1500–60000	-2.6	± 3.5	(stat.)	$^{+0.5}_{-0.5}$	(syst.)
Q^2 range (GeV^2)	$\sigma_{c^{\mathrm{EW}}}$(pb)				
e^+p					
200–1500	9.1	± 4.2	(stat.)	$^{+0.3}_{-1.5}$	(syst.)
1500–60000	-1.4	± 4.3	(stat.)	$^{+0.4}_{-0.3}$	(syst.)
e^-p					
200–1500	-1.7	± 4.1	(stat.)	$^{+0.3}_{-0.3}$	(syst.)
1500–60000	-5.3	± 7.4	(stat.)	$^{+1.1}_{-1.0}$	(syst.)

Table 1: *Cross section σ measurements obtained in each bin with corresponding bin width.*

e^+p	Contribution (%)					
	$200 < Q^2 < 1500\,\mathrm{GeV}^2$			$1500 < Q^2 < 60000\,\mathrm{GeV}^2$		
	$d \to c$	$s \to c$	$\bar{c} \to \bar{s}(\bar{d})$	$d \to c$	$s \to c$	$\bar{c} \to \bar{s}(\bar{d})$
MC	6	36	58	10	26	64
FFN NLO	8	49	43	16	43	41
FONLL-B	8	43	50	12	37	51

e^-p	Contribution (%)					
	$200 < Q^2 < 1500\,\mathrm{GeV}^2$			$1500 < Q^2 < 60000\,\mathrm{GeV}^2$		
	$\bar{d} \to \bar{c}$	$\bar{s} \to \bar{c}$	$c \to s/d$	$\bar{d} \to \bar{c}$	$\bar{s} \to \bar{c}$	$c \to s/d$
MC	3	37	60	2	29	69
FFN NLO	4	51	45	5	49	46
FONLL-B	4	43	54	4	33	63

Table 2: *Contribution of charm subprocesses to EW charm production in CC DIS. The table lists the contributions of the charm production subprocesses in CC DIS in both e^+p and e^-p collisions, as predicted by the MC, Fixed-Flavour Number (FFN) scheme and FONLL-B scheme. The first two columns ($d \to c$ and $s \to c$ for e^+p collisions, for example) reflect the contributions from the QPM processes described in Figure 1 (a) and a higher order correction described in Figure 1 (c). For the MC and FONLL-B scheme, the contribution of the QPM process in Figure 1 (b) enters in the third column ($\bar{c} \to \bar{s}(\bar{d})$) with a higher order correction from the BGF process in Figure 1 (d). For the FFN scheme, the process described in Figure 1 (b) does not participate. Instead, the contribution from the BGF process in Figure 1 (d) is provided in the third column.*

e^+p	MC Contribution (%)			
	$d \to c$	$s \to c$	$\bar{c} \to \bar{s}(\bar{d})$	$g \to c\bar{c}$
Visible kinematic range	9	45	40	6
Full kinematic range	7	31	58	4

e^-p	MC Contribution (%)			
	$\bar{d} \to \bar{c}$	$\bar{s} \to \bar{c}$	$c \to s(d)$	$g \to c\bar{c}$
Visible kinematic range	3	45	40	12
Full kinematic range	2	31	57	10

Table 3: *Contribution of charm subprocesses to charm signal within the visible and full kinematic phase space region. The table lists the contributions of the charm production subprocesses in CC DIS in both e^+p and e^-p collisions as predicted by the MC. The labels in the first three columns are detailed in Table 2. The contribution of the final state gluon splitting described in Fig. 2 enters the fourth column ($g \to c\bar{c}$).*

Q^2 range (GeV^2)	Predictions (pb)							
	FFN ABMP16.3				FONLL-B NNPDF3.1			
	σ	uncertainties			σ	uncertainties		
		PDF	scale	mass		PDF	scale	mass
e^+p								
200 – 1500	4.72	±0.05	$^{+0.31}_{-0.23}$	±0.02	5.37	±0.21	$^{+0.68}_{-0.73}$	±0.00
1500–60000	1.97	±0.03	$^{+0.18}_{-0.13}$	±0.01	2.66	±0.23	$^{+0.37}_{-0.26}$	±0.00
e^-p								
200 – 1500	4.50	±0.05	$^{+0.31}_{-0.23}$	±0.02	4.98	±0.22	$^{+0.66}_{-0.71}$	±0.00
1500–60000	1.73	±0.03	$^{+0.18}_{-0.13}$	±0.01	2.16	±0.22	$^{+0.33}_{-0.21}$	±0.00

Q^2 range (GeV^2)	Predictions (pb)					
	HERAPDF2.0					ATLAS-*epWZ*16
	$f_s = 0.4$ (nominal)	$f_s = 0.3$	$f_s = 0.5$	$f'_s = 0.3$ HERMES	$f'_s = 0.5$ HERMES	
e^+p						
200 – 1500	5.67	5.40	5.96	5.05	5.38	6.41
1500–60000	2.57	2.47	2.65	2.16	2.20	3.07
e^-p						
200 – 1500	5.41	5.15	5.70	4.79	5.12	6.14
1500–60000	2.30	2.21	2.37	1.89	1.93	2.78

Table 4: *List of theory predictions. In the top table are shown the theory predictions from the FFN scheme with ABMP16.3 PDF sets and FONLL-B scheme with NNPDF3.1 PDF sets with their full uncertainties. The ZM-VFNS predictions were generated with HERAPDF2.0 with varied strange quark fraction f_s ranging from 0.3 to 0.5. Additionally, two x-dependent strange quark fractions were used as suggested by the HERMES collaboration. The ZM-VFNS predictions were also evaluated with the ATLAS-epWZ16 PDF sets with an unsuppressed strange quark content as suggested by the ATLAS collaboration.*

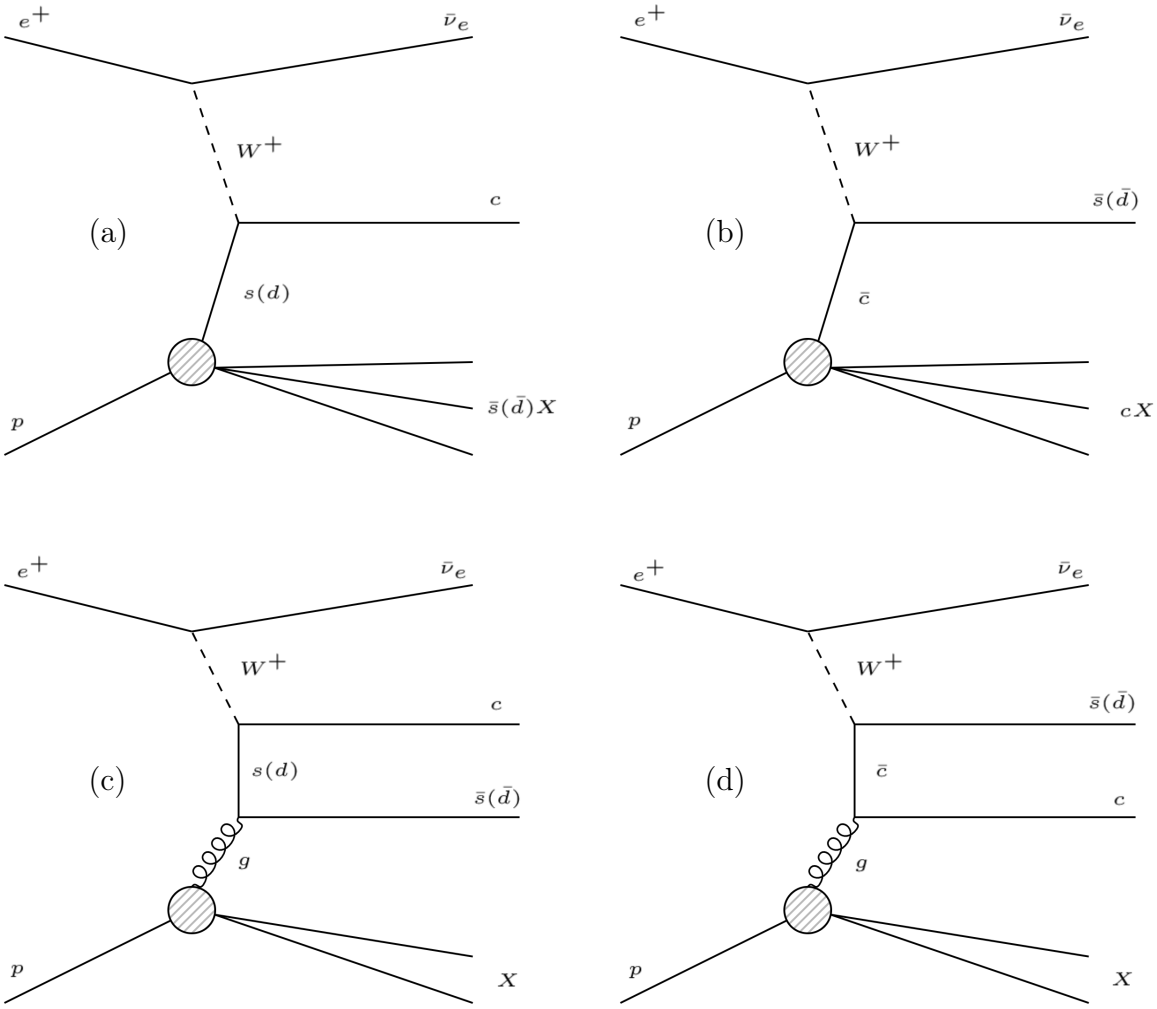

Figure 1: *Feynman diagrams of charm production subprocesses in e^+p collisions. The Quark-Parton model (QPM) process illustrated in (a) describes $s, d \to c$ transition. In the QPM process (b) $\bar{c} \to \bar{s}, \bar{d}$, the charm in the final state arises from the associated charm quark in the proton remnant. In the W boson-gluon fusion processes, the incoming W boson couples to (c) an $s\bar{s}, d\bar{d}$ or (d) a $c\bar{c}$ pair from the gluon in the proton, producing a $c\bar{s}$ pair in the final state.*

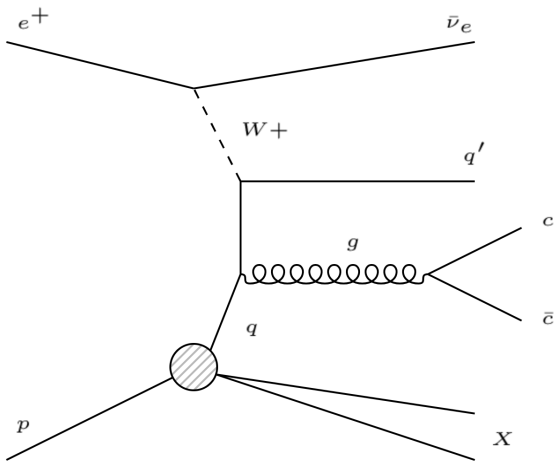

Figure 2: *Feynman diagram of QCD charm process. The $c\bar{c}$ pairs from the final state gluons, illustrated in the figure, are referred to as QCD charm in this analysis. The contribution from this QCD process is included at the charm-quark-tagging stage and later subtracted from the total charm production to obtain the electroweak charm production.*

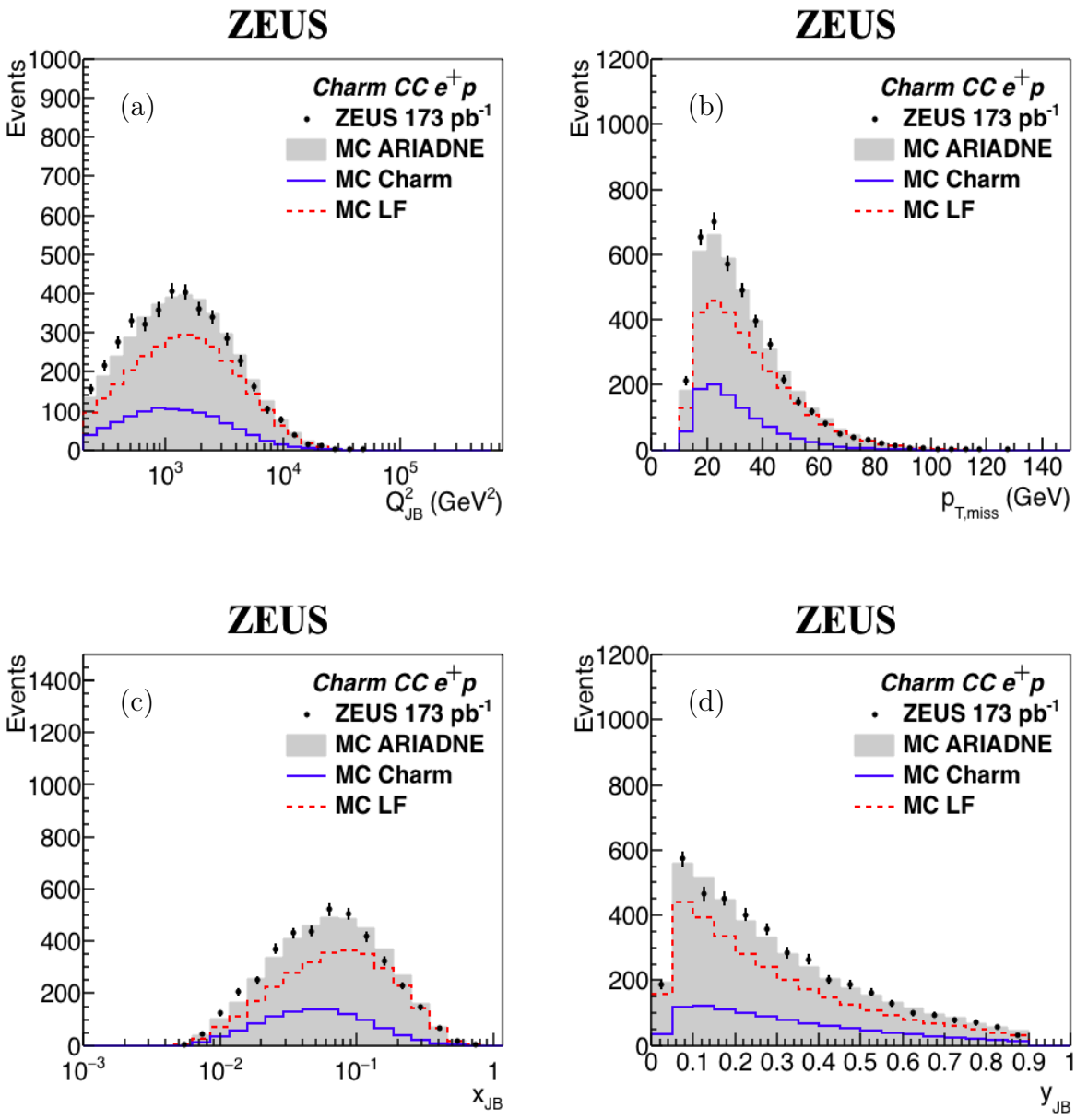

Figure 3: *Comparison between data and MC in kinematic variables (a) Q^2_{JB}, (b) $p_{T,miss}$, (c) x_{JB} and (d) y_{JB} in e^+p collisions. The subscript of the kinematic variables, JB, denotes that these variables are defined using the Jacquet–Blondel method. $p_{T,miss}$ represents missing transverse momentum in the calorimeter. The vertical error bars represent the statistical uncertainty in data. MC Charm represents events with charm or anticharm quarks involved in hard CC reaction either in the initial or final state. MC LF represents the contribution from light-flavored events, i.e. with no heavy flavour particles occurring in the event. MC Beauty represents events with beauty but no charm quark.*

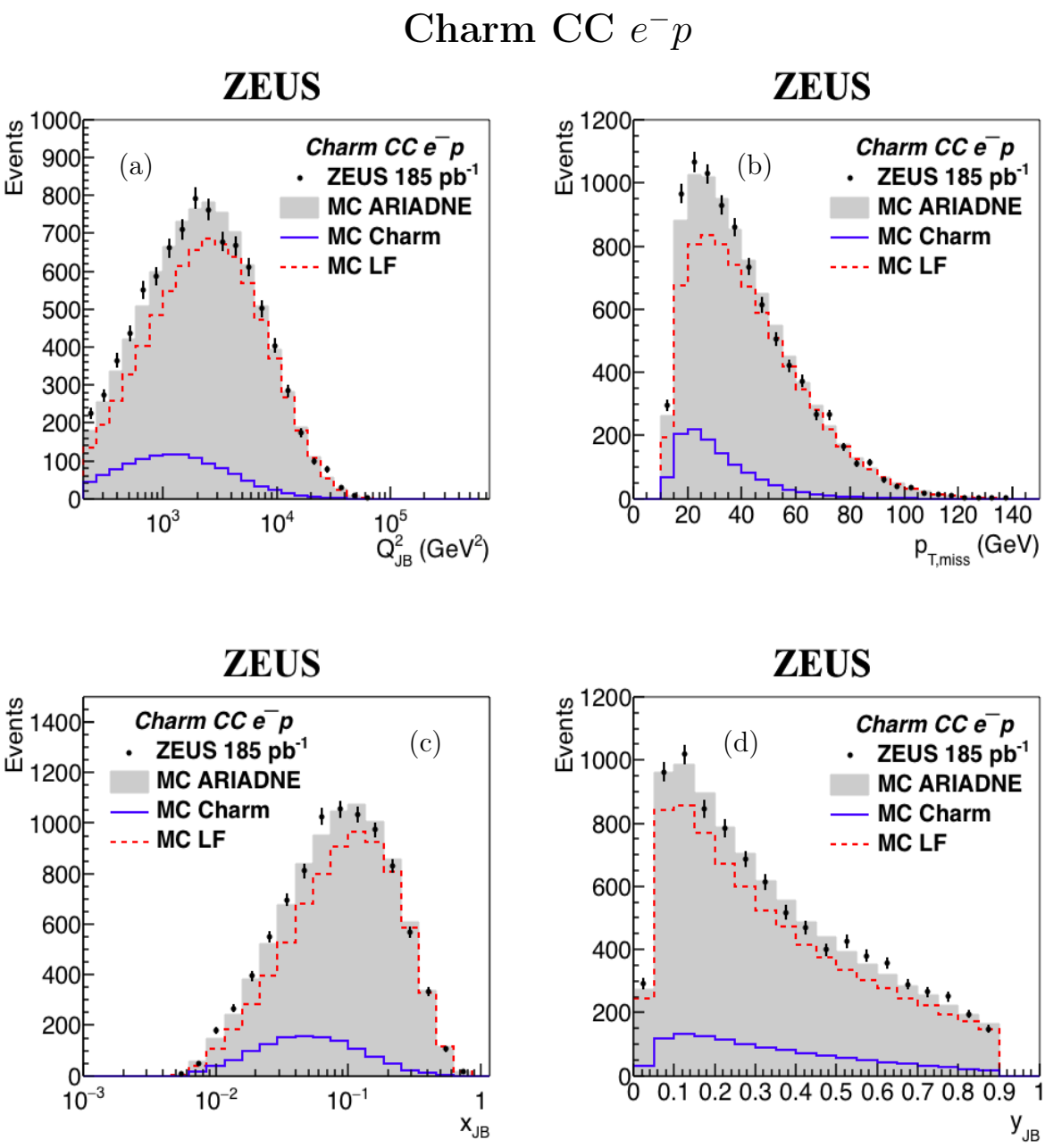

Figure 4: *Comparison between data and MC in kinematic variables (a) Q^2_{JB}, (b) $p_{T,miss}$, (c) x_{JB} and (d) y_{JB} in e^-p collisions. The subscript of the kinematic variables, JB, denotes that these variables are defined using the Jacquet–Blondel method. $p_{T,miss}$ represents missing transverse momentum in the calorimeter. The vertical error bars represent the statistical uncertainty in data. MC Charm represents events with charm or anticharm quarks involved in hard CC reaction either in the initial or final state. MC LF represents the contribution from light-flavored events, i.e. with no heavy flavour particles occurring in the event. MC Beauty represents events with beauty but no charm quark.*

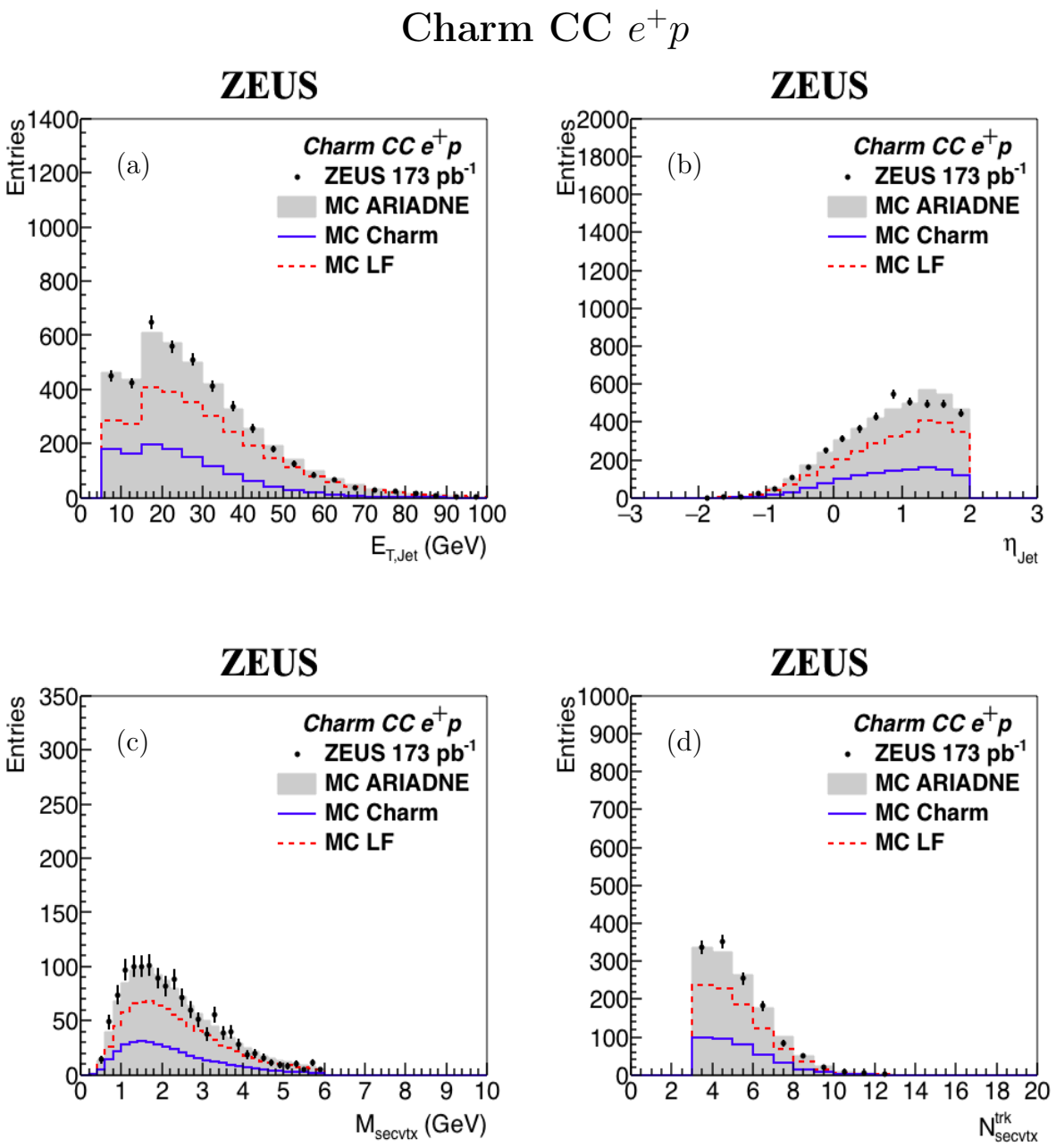

Figure 5: *Comparison between data (points with vertical error bars) and MC in jet and secondary vertex distributions (a) E_T^{jet}, (b) η^{jet}, (c) M_{secvtx} and (d) N^{trk}_{secvtx} in e^+p collisions. The labels are the same as in Figs. 3-4.*

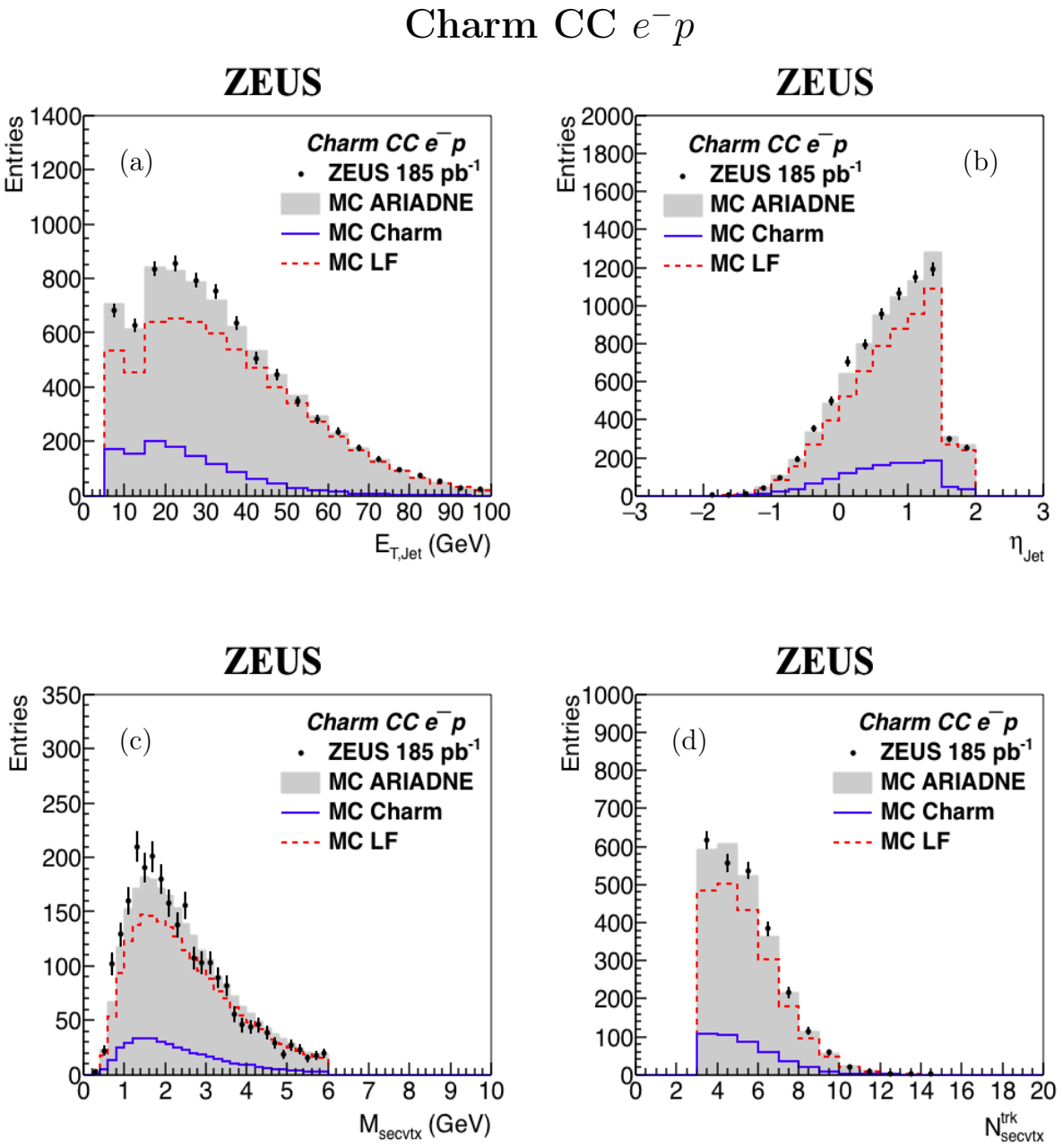

Figure 6: *Comparison between data (points with vertical error bars) and MC in jet and secondary vertex distributions (a) E_T^{jet}, (b) η^{jet}, (c) M_{secvtx} and (d) N^{trk}_{secvtx} in e^-p collisions. The labels are the same as in Figs. 3-4.*

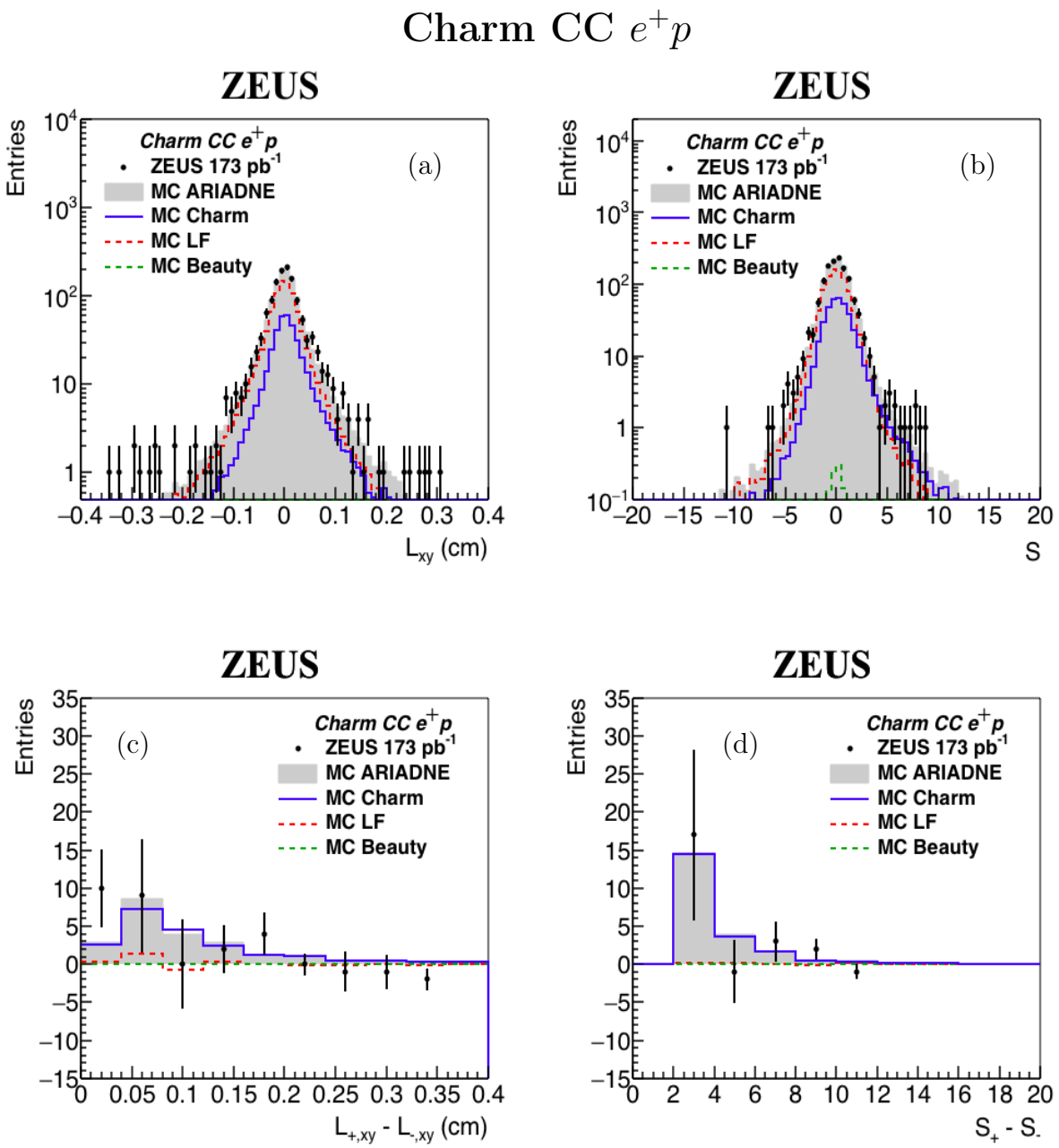

Figure 7: *Charm quark identification by using the lifetime-tagging method. The projected two-dimensional decay length L_{xy} and significance S distributions in e^+p collisions are illustrated in (a) and (b), respectively. The asymmetry of charm quark distribution is visible in these plots. Upon the mirroring of decay length distribution around $L_{xy} = 0$, the light-flavored contribution is suppressed. Charm signal was then extracted by accepting entries with absolute significance $|S| > 2$ from the mirrored decay length and significance distributions, as illustrated in (c) and (d).*

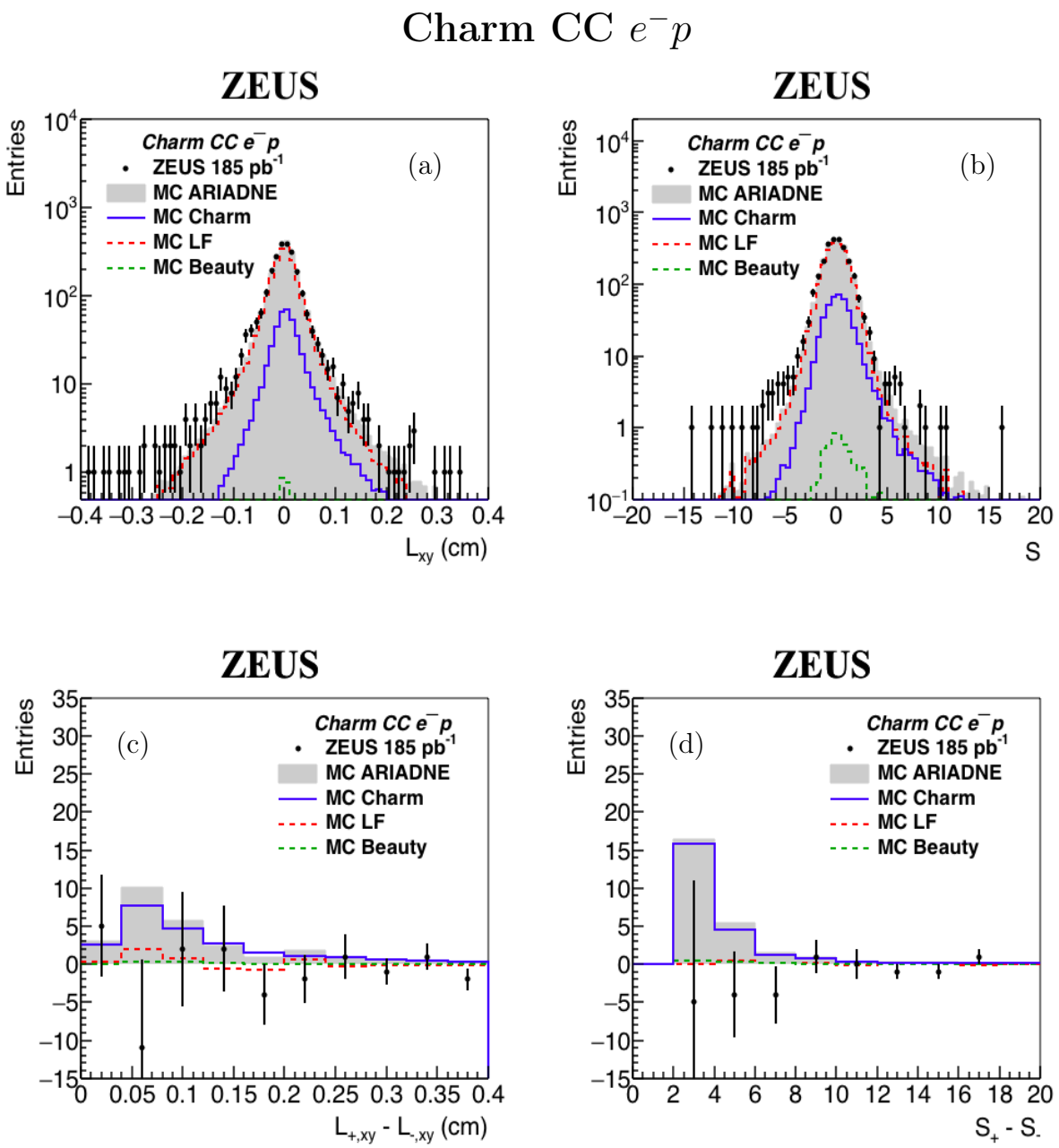

Figure 8: *Charm quark identification by using the lifetime-tagging method. The projected two-dimensional decay length L_{xy} and significance S distributions in e^-p collisions are illustrated in (a) and (b), respectively. The asymmetry of charm quark distribution is visible in these plots. Upon the mirroring of decay length distribution around $L_{xy} = 0$, the light-flavored contribution is suppressed. Charm signal was then extracted by accepting entries with absolute significance $|S| > 2$ from the mirrored decay length and significance distributions, as illustrated in (c) and (d).*

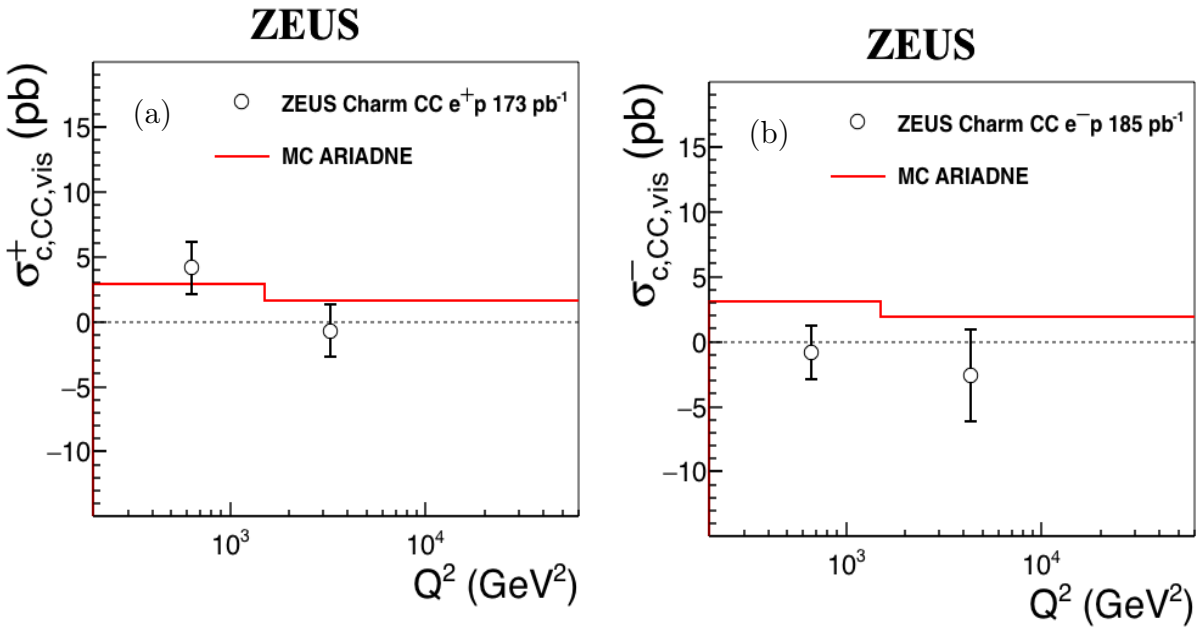

Figure 9: *The total charm cross sections $\sigma_{c,vis}$ within the visible kinematic region in two bins of Q^2 in e^+p (left) and e^-p (right) collisions. The vertical error bars show the statistical uncertainties. The systematic uncertainties are omitted in these plots. The solid red lines represent predictions obtained with the MC.*

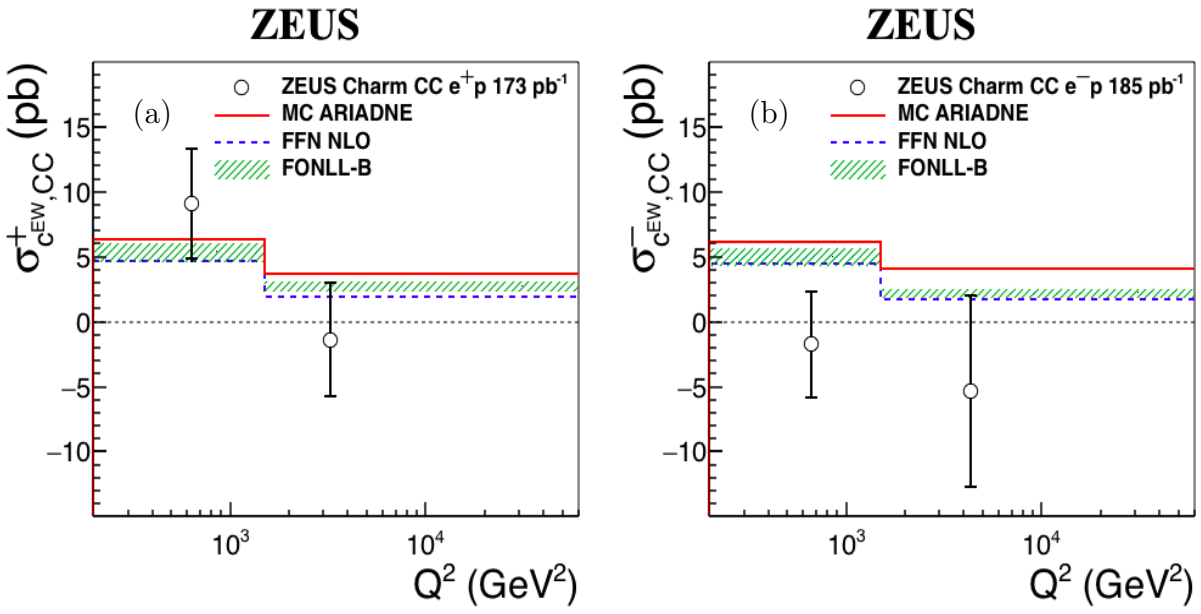

Figure 10: *The EW charm cross sections $\sigma_{c^{EW}}$ in two bins of Q^2 in e^+p (left) and e^-p (right) collisions. The vertical error bars show the statistical uncertainties. The systematic uncertainties are omitted in these plots. The solid red lines represent predictions obtained with the MC. The dashed blue lines represent predictions from FFN scheme with ABMP 16.3 NLO PDF sets. Filled in green hatched band are the total uncertainty in the predictions from FONLL-B schemes with NNPDF3.1 sets around the central value.*